

# Altermagnetism Induced Bogoliubov Fermi Surfaces Form Topological Superconductivity

Bo Fu,<sup>1,\*</sup> Chang-An Li,<sup>2,3,†</sup> and Björn Trauzette<sup>1,3</sup>

<sup>1</sup>*School of Sciences, Great Bay University, Dongguan, China*

<sup>2</sup>*Institute for Theoretical Physics and Astrophysics, University of Würzburg, 97074 Würzburg, Germany*

<sup>3</sup>*Würzburg-Dresden Cluster of Excellence ct.qmat, Germany*

(Dated: December 24, 2025)

We propose a novel type of topological superconductivity based on Bogoliubov Fermi surfaces (BFSs) in an altermagnetic topological insulator proximitized by an *s*-wave superconductor. The 3D altermagnetic topological insulator is characterized by zero-energy surface states in bulk nodal-ring phases and anisotropically shifted surface Dirac cones in topological insulating phases. It is potentially realized in  $\text{EuIn}_2\text{As}_2$ . The altermagnetic order in combination with superconductivity gives rise to highly anisotropic superconducting gaps with crystal-facet-dependent BFSs at the physical boundaries. These particular BFSs provide distinct platforms to realize Majorana zero modes (MZMs). We propose a quasi-1D nanowire in which the anisotropic BFSs experience topological phase transitions due to quantum confinement leading to MZMs at its ends. We further consider vortex phase transitions in the superconducting altermagnetic topological insulators. Remarkably, we find that the altermagnetic order allows us to transit between two distinct type of MZMs, one type is located at the vortex line, while the other type is located at the physical boundaries. Our work paves a new avenue utilizing altermagnetism-induced BFSs to engineer topological superconductivity through crystal anisotropy and quantum confinement.

**Introduction.**—The recent discovery of altermagnets (AMs) has introduced a new type of magnetic phase characterized by momentum dependent spin splitting but with zero net magnetization [1]. It bridges the gap between conventional ferromagnetic and antiferromagnetic phases offering a fertile playground for novel physics and promising applications [1–9]. Extensive research in recent years has been dedicated to their fundamental classification [10–12] and magnetic/electronic properties [13–17]. Crucially, the zero net magnetization in AMs significantly eliminates detrimental stray fields that typically suppress superconducting order while the strong spin splitting is essential for manipulating electronic states [18, 19]. Since no intrinsic superconducting AM has been found so far, it is important to explore if AMs proximitized to conventional *s*-wave superconductors result in topological phases and phenomena [20–25]. Related investigations of AM-superconductor (SC) hybrids have made substantial progress in relation to Andreev reflection [26–28], Josephson effects [29–32], and novel topological phases [33–46]. In particular, the interplay between altermagnetism and topology presents possibilities to realize topological superconductors and MZMs without external fields [47–49]. However, most research efforts have been put into the altermagnetic order in the bulk states, the influence of altermagnetism on topological surface states remains a largely unexplored avenue. Indeed, a critical open question is whether the particular anisotropic features of AMs can be utilized to engineer topological surface states yielding topological superconductivity.

In this work, we directly address this question by demonstrating that it is possible to realize topological superconductivity via topological phase transitions of surface states in altermagnetic topological insulators (AMTIs) in proximity to *s*-wave superconductors. As illustrated in Fig. 1(a), AMTIs are TIs endowed with *d*-wave altermagnetic order, which induces a strong momentum-dependent spin polarization in

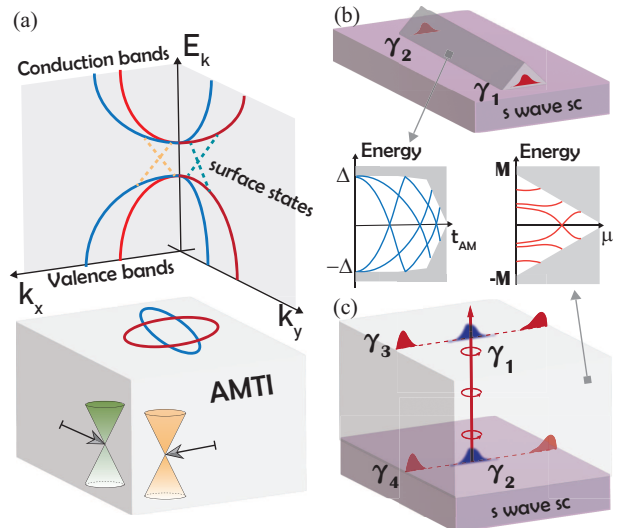


FIG. 1. (a) Schematic of the anisotropic surface states in an AMTI. (b) A quasi-1D triangular prism nanowire of AMTI/SC heterostructure hosting a pair of MZMs at the two ends. The spectrum illustrates the evolution of BFSs to energy levels (blue lines) driven by AM order strength  $t_{AM}$  inside the superconducting gap  $\Delta$ . (c) AMTI/SC hybrid structure with a vortex line, hosting MZMs at vortex core ( $\gamma_{1,2}$ ) or side surfaces ( $\gamma_{3,4}$ ), depending on the value of  $t_{AM}$ . The energy spectrum depicts the evolution of BFSs to discrete surface energy levels (red lines) as a function of chemical potential  $\mu$  within the bulk band gap.

their bulk bands. Consequently, new topological phases such as bulk nodal-ring semimetals appear in AMTIs. The anisotropy of AMs is further imprinted on the topological surface states, where the Dirac cones exhibit a pronounced and facet-dependent momentum shift. When proximitized with an *s*-wave superconductor, the spin-splitting suppresses conventional singlet pairing between time-reversed states. This

leads to the formation of crystal-facet-dependent BFss at the side surfaces, which constitutes the basis for realizing topological superconductivity and MZMs in our proposal. In a prism nanowire geometry, quantum confinement further discretizes the surface BFss into a series of energy levels within the superconducting gap [see Fig. 1(b)]. The altermagnetic order thus acts as a knob to drive topological phase transitions of these surface states, ultimately generating MZMs at the wire ends in nontrivial phases. We further demonstrate that altermagnetic order provides a unique mechanism to exert effective control over vortex-induced MZMs [see Fig. 1(c)]. Notably, the altermagnetic order drives not only vortex phase transitions but also topological phase transitions of BFss at side surfaces, which is beyond the vortex-line physics in conventional superconducting TIs. This transition forces MZMs to migrate from the vortex core to the physical boundaries. Our results provide highly tunable platforms for realizing and controlling topological superconductivity and MZMs by exploiting the profound impact of altermagnetism on topological surface states.

**Model and general analysis.**—We start with a 3D lattice model describing the AMTI proximitized to an *s*-wave superconductor. The corresponding Bogoliubov-de Gennes (BdG) Hamiltonian constructed in the Nambu basis  $\Psi_{\mathbf{k}}^{\dagger} = (C_{\mathbf{k}}^{\dagger}, C_{-\mathbf{k}}^T i\sigma_y)$  takes the form:

$$\mathcal{H}_{\text{BdG}}(\mathbf{k}) = \begin{pmatrix} h(\mathbf{k}) - \mu & \Delta \\ \Delta^* & -\sigma_y h^*(-\mathbf{k}) \sigma_y + \mu \end{pmatrix}, \quad (1)$$

where  $\Delta$  is the superconducting pairing potential,  $\mu$  the chemical potential, and  $\mathbf{k} = (k_x, k_y)$  the Bloch wavevector. The normal-state Hamiltonian  $h(\mathbf{k})$  for the 3D AMTI is given by

$$h(\mathbf{k}) = M(\mathbf{k})\rho_z\sigma_0 + \lambda(\sin k_x\rho_x\sigma_x + \sin k_y\rho_y\sigma_y) + \lambda\sin k_z\rho_z\sigma_z + t_{AM}(\cos k_x - \cos k_y)\rho_z\sigma_z. \quad (2)$$

The Pauli matrices  $\sigma_{\alpha=x,y,z}$  and  $\rho_{\alpha}$  act on spin and orbital degrees of freedom, respectively. The basis takes  $(C_{s\uparrow}, C_{s\downarrow}, C_{p\uparrow}, C_{p\downarrow})^T$ . In Eq. (2), the mass term  $M(\mathbf{k}) \equiv m + t_z \cos k_z + t_{\parallel}(\cos k_x + \cos k_y)$  includes both an orbital energy difference  $m$ , and nearest-neighbor hopping amplitudes  $t_z$  and  $t_{\parallel}$ . The two  $\lambda$  terms refer to spin-orbit coupling. With  $t_{AM} = 0$ ,  $h(\mathbf{k})$  describes a 3D TI classified by weak, strong, and trivial insulating phases [50–52]. The term  $t_{AM}(\cos k_x - \cos k_y)\rho_z\sigma_z$  represents a *d*-wave altermagnetic order with field strength  $t_{AM}$  [53]. It is similar to the altermagnetic order recently introduced in 2D quantum spin Hall insulators [37–40].

Before discussing the superconducting phase, it is instructive to analyze the properties of the normal-state Hamiltonian  $h(\mathbf{k})$  of the topological AMs. With  $t_{AM} \neq 0$ , the altermagnetic order profoundly influences the original properties of the TIs. Importantly, it modifies the symmetry of the system. The altermagnetic order breaks both time-reversal symmetry  $T$  and four-fold rotation symmetry  $C_{4z}$  individually, but preserves their combined operation  $C_{4z}T$ . This reduced symmetry shift the system from the magnetic point group  $4/mmm1'$

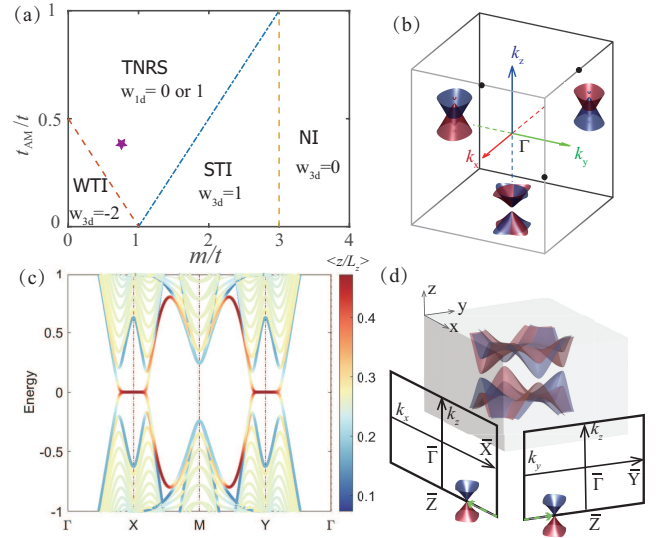


FIG. 2. (a) Phase diagram of the AMTI in the parameter space of  $m$  and  $t_{AM}$ . The four different phases are weak topological insulators (WTIs), strong topological insulators (STIs), normal insulators (NIs), and topological nodal-ring semimetals (TNRS), respectively. (b) 3D Brillouin zone and band structure for TNRS [purple hexagon in (a)] near the high-symmetry points  $(\pi, 0, \pi)$ ,  $(0, \pi, \pi)$  and  $(\pi, \pi, 0)$  (marked by black dots). The plots show the band dispersion for  $k_z = 0$  or  $\pi$ . Red and blue colors denote the horizontal mirror eigenvalues  $\sigma_h = +i$  and  $-i$ , respectively. (c) Band structure of a thin-film topological AM in the  $xy$ -plane with width  $L_z = 20$ , plotted along high-symmetry lines. Parameters:  $t_{AM} = 0.4$ ,  $\lambda = 1$ , and  $m = 0.8$ . (d) Schematic of the AM-induced anisotropic shift of surface Dirac cone on (010) and (100) side surfaces in the STI phase.

to  $4'/m'm'm'$ , resulting in an anisotropic Fermi surface [see Fig. 2(b)] and momentum-dependent spin polarization [54]. Additionally, the altermagnetic order affect the topological properties and band structure significantly. The modified phase diagram is presented in Fig. 2(a). The anisotropic nature of the altermagnetic order makes it act differently on the high-symmetry points (HSPs) of the Brillouin zone. Near the  $(\pi, 0, \pi)$  and  $(0, \pi, \pi)$  points, it acts as a constant Zeeman field  $\sim 2t_{AM}\rho_z\sigma_z$ , lifting the spin degeneracy. While near the  $(\pi, \pi, 0)$  point, it takes *d*-wave form  $\sim \frac{t_{AM}}{2}(\delta k_x^2 - \delta k_y^2)\rho_z\sigma_z$  (where  $\delta k_i$  is the momentum deviation from the HSP), preserving band degeneracy at this point but splitting bands away from it. When  $2t_{AM} > |M(\mathbf{k}) - t|$ , the band inversion near  $(\pi, 0, \pi)$  and  $(0, \pi, \pi)$  creates a nodal structure in the  $k_z = \pi$  plane, yielding a topological nodal-ring semimetal phase [see Figs. 2(a) and 2(b)]. Its topology is captured by the 1D winding number and manifested by zero-energy states at boundaries as shown in Fig. 2(c) [55]. Due to the presence of chiral symmetry  $C = \rho_y$ , the gapped phases are characterized by the 3D winding number  $w_{3D}$  [56]. This invariant distinguishes the topological phases:  $w_{3D} = 1$  for STI,  $w_{3D} = -2$  for WTI, and  $w_{3D} = 0$  for NI (see End Matter).

Notably, the anisotropic nature of AMs strongly affects the topological surface states. For concreteness, we focus on the STI phase of the phase diagram Fig. 2(a) in the

following. A low-energy expansion near the  $(\pi, \pi, \pi)$  point demonstrates that the altermagnetic term takes the form  $\sim t_{AM}(\delta k_x^2 - \delta k_y^2)\rho_z\sigma_z$ . On certain side surfaces, such as the (100) and (010) facets, the altermagnetic order acts as a direction-dependent Zeeman field, shifting the Dirac cones in an anisotropic way [see Fig. 2(d)]. For instance, the effective Hamiltonian for the (010) surface is given by:  $h_{010} = \lambda[(-\delta k_x + k_{AM})\sigma_x - \delta k_z\sigma_y]$  with  $k_{AM} \equiv -\frac{t_{AM}}{t}\frac{(M-3t)}{\lambda}$  [54]. In contrast, the projection of the AM term vanishes on (110),  $(\bar{1}10)$  and (001) surfaces, leaving their Dirac cones intact. This is crucial for the formation of BFSs and the realization of topological superconductivity, as we discuss below.

In the presence of superconductivity, the system possesses particle-hole symmetry  $\Xi = \tau_y\sigma_y K$  where  $K$  is complex conjugation. A finite chemical potential breaks chiral symmetry explicitly, placing the system in the topologically trivial class D for 3D gapped systems. However, the altermagnetic order can induce gapless bulk and surface states, which host non-trivial topology. For the bulk states, the altermagnetic spin splitting prohibits the formation of conventional spin-singlet Cooper pairs between time-reversed states at  $\mathbf{k}$  and  $-\mathbf{k}$ . This leads to a superconducting state with a gapless quasiparticle spectrum [57], manifested as bulk BFSs [58–63]. However, we are more interested in the surface bands, when the chemical potential lies in the bulk band gap. With a superconducting gap  $\Delta$ , the surface spectrum for the (100) surface at  $\delta k_z = 0$  becomes:  $E_{s,\zeta}^{100} = s\lambda k_{AM} + \zeta\sqrt{\Delta^2 + (\mu + s\lambda\delta k_y)^2}$ , where  $s, \zeta = \pm 1$ . While for the (110) surface, its spectrum remains intact as  $E_{s,\zeta}^{110} = \zeta\sqrt{\Delta^2 + (\mu + s\lambda\delta k')^2}$ . The local density of states calculated for a semi-infinite system [64] for these two cases are shown in Figs. 3(a) and 3(b), respectively. For the (100) facet, there exists a critical altermagnetic strength  $t_c^s = \frac{\Delta t}{|M-3t|}$ , beyond which the surface BFSs form [see Fig. 3(a)]. In contrast, there is a direct superconducting gap for the (110) facet [see Fig. 3(b)].

*Engineering topological superconductivity via surface anisotropy with altermagnetic order.*—Considering the setup in Fig. 1(b), we now demonstrate how the anisotropic surface properties and associated BFS can be exploited to obtain a topological superconducting phase hosting MZMs. The quasi-1D nanowire is extended along  $z$ -direction. We use a triangular prism geometry bounded by (110),  $(\bar{1}10)$ , and (010) crystallographic facets, which breaks  $C_{4z}T$  symmetry lifting degeneracies. To investigate the topological properties of this system, we assume the nanowire has a finite width  $L_x$  in the (010) facet and infinite length in  $z$  direction. Henceforth,  $k_z$  is a good quantum number. Due to quantum confinement, the BFSs at surface (100) evolve to different energy bands as a function  $k_z$  within the superconducting gap  $\Delta$ . This is because the BFSs on the (010) facet are bounded by gapped surface states on the (110) and  $(\bar{1}10)$  facets with a finite superconducting gap. The topological property of this quasi-1D system is characterized by a  $\mathbb{Z}_2$  invariant in class D, enabled by the presence of particle-hole symmetry [56]. The topological phase transition is determined by the gap closing at  $k_z = \pi$ ,

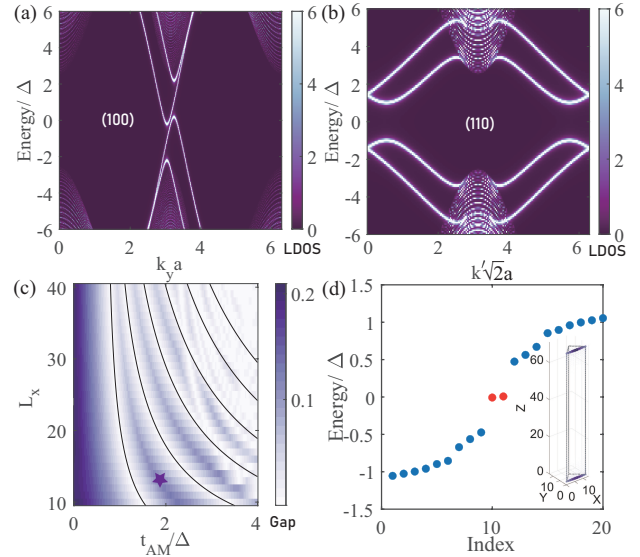


FIG. 3. (a, b) Local density of states on (010) and (110) surfaces at  $k_z = \pi$ , calculated from the surface Green's function. (c) Topological phase diagram for a triangular prism geometry with surfaces (110),  $(\bar{1}10)$ , and (010). The color map represents the energy gap obtained from numerical diagonalization of the quasi-1D nanowire at  $k_z = \pi$ , plotted as a function of  $L_x$  and  $t_{AM}$ . Black curves indicate phase boundaries obtained from analytical solutions. (d) Energy spectra for quasi-1D nanowire of length  $L_z = 80$ . The red dots indicate MZMs. The inset shows the spatial profile of the MZMs. Other Parameters are:  $m = 1.5$ ,  $\mu = 0.1$ ,  $\lambda = 1$ , and  $\Delta = 0.1$ .

which is tuned by both the size  $L_x$  and strength  $t_{AM}$ .

The gap-closing conditions for topological phase transitions can be obtained by employing a low-energy effective theory of surface states [54], which yields

$$L_x/\xi = \frac{n\pi - \arctan \sqrt{(k_{AM}\xi)^2 - 1}}{\sqrt{(k_{AM}\xi)^2 - 1}}, \quad (3)$$

where  $\xi = \lambda/\Delta$  is the superconducting coherence length,  $k_{AM} = -\frac{t_{AM}}{t}\frac{(M-3t)}{\lambda}$ , and  $n$  is an integer taking  $n = 1, 2, 3, \dots$ . This equation determines the phase boundaries between trivial and topological superconductors in the parameter space  $(t_{AM}, L_x)$ , as shown by solid lines in Fig. 3(c). Note that this equation is consistent with the result obtained from Andreev scattering method [65]. We can directly compare the analytical results with numerical simulations. The energy gap obtained from a tight-binding model is presented in Fig. 3(c). The quasi-1D nanowire exhibits a series of gap closings and re-openings, indicating multiple topological phase transitions. The excellent agreement between these analytical results and numerics confirms the above analysis of phase transitions.

We further examine the topological nature of the system by showing the appearance of MZMs driven by altermagnetic orders. Let us focus on the first topological phase region between  $n = 1$  and  $n = 2$  with a topological invariant  $\mathbb{Z}_2 = 1$  [66], as shown in Fig. 3(c). We impose open boundary con-

ditions along  $z$  direction and take a finite length  $L_z$ . The obtained eigenenergies near zero energy are plotted in Fig. 3(d). A pair of MZMs is found to reside at the band center, with a protecting gap as large as the original superconducting gap  $\Delta$ . This large gap provides advantages avoiding the fine tuning of parameters. The corresponding wave functions are shown in the inset of Fig. 3(d), which indicates that the hosted MZMs localize at the two ends of quasi-1D nanowire of finite length as expected.

**Altermagnetic control of MZMs in a vortex line.**—Next, we consider the setup in Fig. 1(c) and show the control of MZMs in the vortex lines by altermagnetic order. We can implement a  $\pi$ -flux vortex line along  $z$ -direction, described by the order parameter  $\Delta \tanh(r/\xi) e^{i\theta_r}$  where  $r = \sqrt{x^2 + y^2}$  and  $\theta_r$  is the phase angle and  $\xi$  the coherence length. The vortex line breaks translational symmetry in the  $xy$ -plane but keeps  $k_z$  a good quantum number. With a finite cross-section in the  $xy$ -plane, the system hosting a vortex line can be treated as quasi-1D, allowing us to study its topological properties.

We obtain the energy spectrum of this quasi-1D system by diagonalizing the tight-binding BdG Hamiltonian. The topological phase transition is captured by the gap closing at  $k_z = \pi$ . The topological phase diagram with corresponding gap values in parameter space  $(t_{AM}, \mu)$  is presented in Fig. 4(a). The color scale represents the band gap of the energy spectrum at  $k_z = \pi$ . This phase diagram is divided into four distinct phase regions, labeled as (I) to (IV). The topological properties of the gapped regions can be characterized by a pair of winding numbers  $\mathbb{Z}_{+i} \oplus \mathbb{Z}_{-i} \equiv (w_{+i}, w_{-i})$ , which are defined as follows. Despite the breaking of time reversal symmetry  $T$  due to the presence of the vortex line, the system retains a modified symmetry resembling time reversal, i.e., the combined operation  $\sigma_v T$ , where  $\sigma_v$  denotes the vertical mirror reflection with respect to the  $xz$  or  $yz$ -plane. The chiral symmetry  $C_v$  can be further constructed from the particle-hole symmetry  $\Xi$  and  $\sigma_v T$ , given by  $C_v = \tau_z \rho_z \sigma_z$  incorporating the mirror reflection with  $C_v^2 = 1$ . Furthermore, since  $[C_v, C_{2z}] = 0$ , a winding number can be defined within each eigensector of the two-fold rotation  $C_{2z}$ . Consequently, the quasi-1D vortex system is characterized by a pair of winding numbers  $(w_{+i}, w_{-i})$ , where the subscript denotes the  $C_{2z}$  eigenvalue [67–70]. These invariants determine the presence or absence of MZMs at the two ends the quasi-1D system.

The four phase regions shown in Fig. 4(a) demonstrate different topological properties and band gaps. Explicitly, they are classified as: (I) Majorana vortex phase at small  $\mu$  and small  $t_{AM}$ , in which the vortex line is topological nontrivial and hosts MZMs at its ends; (II) trivial vortex phase at large  $\mu$  and small  $t_{AM}$ , in which the vortex line is trivial; (III) bulk nodal phase for  $t_{AM} > t_c^b$  with  $t_c^b = \frac{1}{2} \sqrt{\Delta^2 + (\mu - |M - t|)^2}$ , in which the bulk bands develop BFSs; and (IV) surface nodal vortex phase for  $t_c^b > t_{AM} > t_c^s$ . In this particular phase (IV), the system has an oscillating band gap while hosting MZMs at the surface boundaries. We mainly focus on the properties of nontrivial regions (I) and (IV) in the following [71].

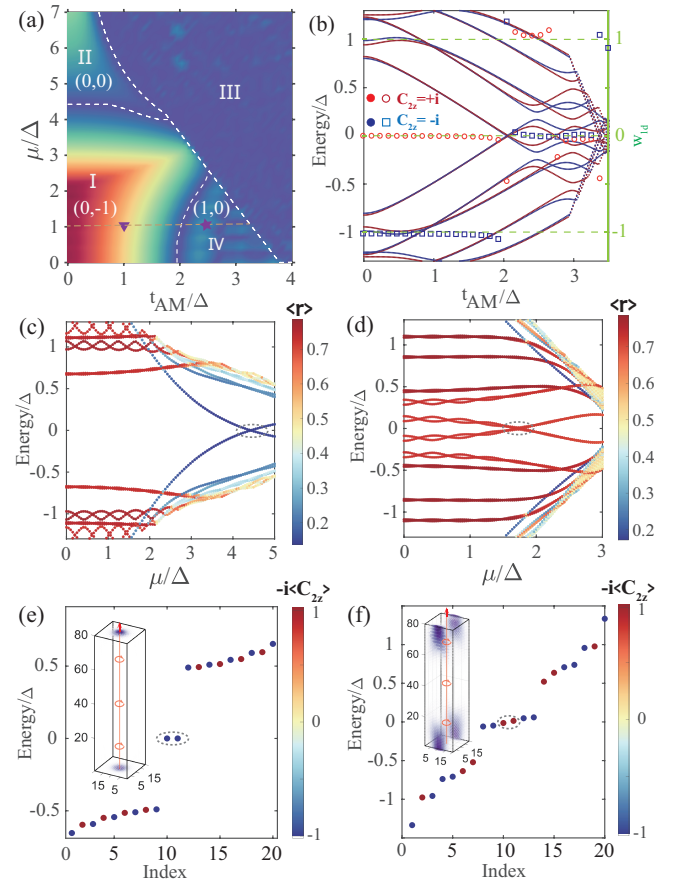


FIG. 4. (a) Topological phase diagram in the parameter space of altermagnetic strength  $t_{AM}$  and chemical potential  $\mu$  for a vortex line along the  $z$ -axis. Roman numerals label distinct phases: (I) Majorana vortex phase, (II) trivial vortex phase, (III) bulk nodal phase, and (IV) surface nodal phase. The color scale represents the energy gap near zero energy. (b) Energy spectrum  $E(k_z = \pi)$  as a function of  $t_{AM}$  at a fixed chemical potential  $\mu/\Delta = 1$  [horizontal dashed line in (a)]. Red and blue lines denote states in  $C_{2z} = +i$  and  $-i$  eigensectors, with squares and circles marking the corresponding topological winding numbers  $(w_{+i}, w_{-i})$ . (c, d) Energy spectrum  $E(k_z = \pi)$  as a function of  $\mu$  for a fixed altermagnetic strength: In (c)  $t_{AM}/\Delta = 0.5$  and in (d)  $t_{AM}/\Delta = 2.3$ . The color of each data point indicates the spatial localization of the corresponding state, quantified by its average distance from the vortex core  $\langle r \rangle$  (red: outer surface states; blue: vortex core-bound states). (e, f) Energy spectrum with open boundary conditions along  $z$ -direction ( $L_z = 80$ ) and spatial profile of the corresponding MZMs (inset) for parameters marked in (a): (e)  $t_{AM}/\Delta = 1$  (triangle), (f)  $t_{AM}/\Delta = 2.4$  (hexagon). Parameters for all panels:  $L_x = L_y = 20$ ,  $m = 2.5$ ,  $\lambda = 1$ , and  $\Delta = 0.2$ .

The vortex phase transition can be induced by the altermagnetic order strength  $t_{AM}$  and chemical potential  $\mu$ . At fixed chemical potential  $\mu/\Delta = 1$ , the low-energy spectrum of the quasi-1D system as a function of  $t_{AM}$  is shown in Fig. 4(b) [horizontal dashed line in Fig. 4(a)]. The spectra for  $C_{2z} = +i$  and  $-i$  eigensectors are depicted in red and blue, respectively. Note that eigenstates from different  $C_{2z}$  sectors will not hybridize due to the symmetry protection. As  $t_{AM}$  increases, the

spectral gaps in both sectors close near  $t_{AM}/\Delta = 2 \simeq t_c^b$ , indicating a topological phase transition. This transition is also confirmed by the jump of the winding numbers ( $w_{+i}, w_{-i}$ ) from  $(0, -1)$  to  $(1, 0)$ , annotated by square and circle symbols, respectively. To understand the vortex phase transitions and surface phase transition of BFSs at the outer surfaces, we plot the spectra of the quasi-1D system at  $k_z = \pi$  as a function of  $\mu$  for different  $t_{AM}$  in Figs. 4(c) and 4(d), respectively. The corresponding color scale represents the spatial localization of the eigenstates, ranging from the vortex core (blue color) to the outer surface (red color).

In the subcritical regime with  $t_{AM} < t_c^b$  [see Fig. 4 (c)], the primary low-energy physics and topological phase transitions are governed by the vortex line. At small  $\mu$ , the vortex line is topological nontrivial and hosts a pair of MZMs at its two ends [72–74]. This topological characterization persists as  $\mu$  increases into the bulk states until a topological phase transition occurs at the point marked by the gray circle in Fig. 4(c). Intriguingly, discrete low-energy states appear within the superconducting gap in this phase (at small  $\mu$ ), which are bound to the side surfaces rather than the vortex line. In stark contrast, in the supercritical regime with  $t_{AM} > t_c^b$  [see Fig. 4 (d)], the dominant physics and topological phase transitions shift to the outer side surfaces. Due to the quantum confinement in the  $xy$ -plane, the surface BFSs are quantized to discrete energy levels within the superconducting gap  $\Delta$ . The introduction of a  $\pi$ -flux vortex line breaks the  $C_{4z}T$  symmetry and lifts the double degeneracy of energy bands. This lifting of degeneracy ultimately endows a novel topological phase transition [gray circle in Fig. 4(d)] of BFSs at the outer side surface as changing  $\mu$ . Note that there is no band crossing at the vortex line in this case.

Finally, we present the energy spectra and corresponding probability density of MZMs under open boundary conditions for the two distinct topological phases. For the phase region (I) with winding numbers  $(w_{+i}, w_{-i}) = (0, -1)$ , indicated by a triangle in Fig. 4(a), the MZMs are localized at the vortex line [see Fig. 4(e)], consistent with the Fu-Kane proposal [72, 75]. In contrast, for the phase region (IV)  $(w_{+i}, w_{-i}) = (1, 0)$ , represented by the hexagon in Fig. 4(a), the MZMs are localized at the outer surface [see Fig. 4(f)] [76]. It is interesting to note that the  $C_{2z}$  eigenvalues corresponding to MZMs of these two cases are also switched. This result demonstrates that the altermagnetic order drives a topological phase transition which relocates MZMs from the vortex line core to the outer side surfaces.

**Discussion and conclusions.**—We propose a fundamentally new way to realize topological superconductivity utilizing the unique interplay between  $d$ -wave AMs, topology, and  $s$ -wave superconductivity. Our proposal is based on particular features of this combination: (i) Crystal-facet-dependent anisotropy: The surface BFSs at different physical boundaries are anisotropic. Thus, quantum confinement decisively affects the topological phase. (ii) Stray field free and zero net magnetization: There is no need for external magnetic fields, which excludes detrimental stray field that jeopardizes superconduc-

tivity and scalability. (iii) Vortex-line based Majorana manipulation: We demonstrate how MZMs move from the vortex line to the side surfaces driven by the altermagnetic order via a topological phase transition.

Our proposal could be realized in  $\text{EuIn}_2\text{As}_2$  in proximity to an ordinary  $s$ -wave superconductor. This material is a promising candidate for an intrinsic AMTI, since it is predicted to exhibit both a topological insulating phase as well as altermagnetic order [77, 78]. Alternatively, our proposal could also be realized in a heterostructure consisting of AM-TI-SC, utilizing the proximity effect of both altermagnetic and superconducting order. There are several available AM materials including  $\text{KV}_2\text{Se}_2\text{O}$  [79],  $\text{Rb}_{1-\delta}\text{V}_2\text{Te}_2\text{O}$  [80], and  $\text{Mn}_5\text{Si}_3$  [81, 82], that could be brought in proximity to 3D TIs and  $s$ -wave superconductors.

**Acknowledgments.**—We thank J. Li for helpful discussions. B.F. was financially supported by National Natural Science Foundation of China (Grants No.12504049), Guangdong Province Introduced Innovative R&D Team Program (Grant No. 2023QN10X136), Guangdong Basic and Applied Basic Research Foundation No. 2024A1515010430 and 2023A1515140008), Quantum Science Center of Guangdong-Hong Kong-Macao Greater Bay Area (Grant No. GDZX230005). C.A.L. and B.T. were supported by the DFG (SFB 1170 ToCoTronics), and the Würzburg-Dresden Cluster of Excellence ct.qmat, EXC 2147 (Project-Id 390858490).

\* fubo@gbu.edu.cn

† changan.li@uni-wuerzburg.de

- [1] L. Šmejkal, J. Sinova, and T. Jungwirth, *Phys. Rev. X* **12**, 040501 (2022).
- [2] M. Naka, S. Hayami, H. Kusunose, Y. Yanagi, Y. Motome, and H. Seo, *Nat. Commun.* **10**, 4305 (2019).
- [3] S. Hayami, Y. Yanagi, and H. Kusunose, *J. Phys. Soc. Jpn.* **88**, 123702 (2019).
- [4] L. Šmejkal, R. González-Hernández, T. Jungwirth, and J. Sinova, *Sci. Adv.* **6**, eaaz8809 (2020).
- [5] D.-F. Shao, S.-H. Zhang, M. Li, C.-B. Eom, and E. Y. Tsymbal, *Nat. Commun.* **12**, 7061 (2021).
- [6] L. Šmejkal, J. Sinova, and T. Jungwirth, *Phys. Rev. X* **12**, 031042 (2022).
- [7] L. Bai, W. Feng, S. Liu, L. Šmejkal, Y. Mokrousov, and Y. Yao, *Adv. Funct. Mater.* **34**, 2409327 (2024).
- [8] M. Gu, Y. Liu, H. Zhu, K. Yananose, X. Chen, Y. Hu, A. Stroppa, and Q. Liu, *Phys. Rev. Lett.* **134**, 106802 (2025).
- [9] C. Song, H. Bai, Z. Zhou, L. Han, H. Reichlova, J. H. Dil, J. Liu, X. Chen, and F. Pan, *Nat. Rev. Mater.* **10**, 473 (2025).
- [10] P. Liu, J. Li, J. Han, X. Wan, and Q. Liu, *Phys. Rev. X* **12**, 021016 (2022).
- [11] Z. Xiao, J. Zhao, Y. Li, R. Shindou, and Z.-D. Song, *Phys. Rev. X* **14**, 031037 (2024).
- [12] J. Yang, Z.-X. Liu, and C. Fang, *Nat. Commun.* **15**, 10203 (2024).
- [13] C. R. W. Steward, R. M. Fernandes, and J. Schmalian, *Phys. Rev. B* **108**, 144418 (2023).
- [14] R. M. Fernandes, V. S. de Carvalho, T. Birol, and R. G. Pereira, *Phys. Rev. B* **109**, 024404 (2024).

[15] Y. Yu, T. Shishidou, S. Sumita, M. Weinert, and D. F. Agterberg, *Proc. Natl. Acad. Sci. U.S.A.* **121**, e2411038121 (2024).

[16] Y. Fang, J. Cano, and S. A. A. Ghorashi, *Phys. Rev. Lett.* **133**, 106701 (2024).

[17] C. Autieri, R. M. Sattigeri, G. Cuono, and A. Fakhredine, *Phys. Rev. B* **111**, 054442 (2025).

[18] M. G. Blamire and J. W. A. Robinson, *J. Phys. Condens. Matter.* **26**, 453201 (2014).

[19] K. Parshukov and A. P. Schnyder, arXiv preprint arXiv:2507.10700 (2025).

[20] C. W. J. Beenakker and T. Vakhtel, *Phys. Rev. B* **108**, 075425 (2023).

[21] M. Wei, L. Xiang, F. Xu, L. Zhang, G. Tang, and J. Wang, *Phys. Rev. B* **109**, L201404 (2024).

[22] H. G. Giil and J. Linder, *Phys. Rev. B* **109**, 134511 (2024).

[23] B. Lu, P. Mercebach, P. Burset, K. Yada, J. Cayao, Y. Tanaka, and Y. Fukaya, arXiv preprint arXiv:2508.03364 (2025).

[24] Y. Nagae, L. Katayama, and S. Ikegaya, *Phys. Rev. B* **111**, 174519 (2025).

[25] N. Heinsdorf and M. Franz, arXiv preprint arXiv:2509.03774 (2025).

[26] C. Sun, A. Brataas, and J. Linder, *Phys. Rev. B* **108**, 054511 (2023).

[27] C. W. J. Beenakker and T. Vakhtel, *Phys. Rev. B* **108**, 075425 (2023).

[28] M. Papaj, *Phys. Rev. B* **108**, L060508 (2023).

[29] J. A. Ouassou, A. Brataas, and J. Linder, *Phys. Rev. Lett.* **131**, 076003 (2023).

[30] H.-P. Sun, S.-B. Zhang, C.-A. Li, and B. Trauzettel, *Phys. Rev. B* **111**, 165406 (2025).

[31] K. Maeda, B. Lu, K. Yada, and Y. Tanaka, *J. Phys. Soc. Jpn.* **93**, 114703 (2024).

[32] S.-B. Zhang, L.-H. Hu, and T. Neupert, *Nat. Commun.* **15**, 1801 (2024).

[33] D. Zhu, Z.-Y. Zhuang, Z. Wu, and Z. Yan, *Phys. Rev. B* **108**, 184505 (2023).

[34] J.-Y. Zou, B. Fu, and S.-Q. Shen, *Commun. Phys.* **7**, 275 (2024).

[35] M. Ezawa, *Phys. Rev. B* **110**, 165429 (2024).

[36] M.-H. Zhang, L. Xiao, and D.-X. Yao, arXiv preprint arXiv:2407.18379 (2024).

[37] H.-Y. Ma and J.-F. Jia, *Phys. Rev. B* **110**, 064426 (2024).

[38] R. González-Hernández, H. Serrano, and B. Uribe, *Phys. Rev. B* **111**, 085127 (2025).

[39] Y.-Y. Li and S.-B. Zhang, *Phys. Rev. B* **111**, 045106 (2025).

[40] R. Gonzalez-Hernandez and B. Uribe, arXiv preprint arXiv:2507.23173 (2025).

[41] Z. Chen, F. Zhan, D.-S. Ma, D.-H. Xu, and R. Wang, arXiv preprint arXiv:2508.03580 (2025).

[42] D. S. Antonenko, R. M. Fernandes, and J. W. F. Venderbos, *Phys. Rev. Lett.* **134**, 096703 (2025).

[43] R. Chen, Z.-M. Wang, K. Wu, H.-P. Sun, B. Zhou, R. Wang, and D.-H. Xu, *Phys. Rev. Lett.* **135**, 096602 (2025).

[44] Z. Li, Z. Li, and Z. Qiao, *Phys. Rev. B* **111**, 155303 (2025).

[45] N. Heinsdorf, *Phys. Rev. B* **111**, 174407 (2025).

[46] Y.-H. Wan and Q.-F. Sun, *Phys. Rev. B* **111**, 045407 (2025).

[47] S. A. A. Ghorashi, T. L. Hughes, and J. Cano, *Phys. Rev. Lett.* **133**, 106601 (2024).

[48] Y.-X. Li, *Phys. Rev. B* **109**, 224502 (2024).

[49] Y.-X. Li, Y. Liu, and C.-C. Liu, *Phys. Rev. B* **109**, L201109 (2024).

[50] L. Fu and C. L. Kane, *Phys. Rev. B* **76**, 045302 (2007).

[51] L. Fu, C. L. Kane, and E. J. Mele, *Phys. Rev. Lett.* **98**, 106803 (2007).

[52] H. Zhang, C.-X. Liu, X.-L. Qi, X. Dai, Z. Fang, and S.-C. Zhang, *Nat. Phys.* **5**, 438 (2009).

[53] Note that the altermagnetic term starkly contrasts with the  $(\cos k_x - \cos k_y)\rho_y\sigma_0$  term in higher-order topological insulators [?], although both terms share the same symmetry. The  $(\cos k_x - \cos k_y)\rho_y\sigma_0$  term gaps all side Dirac cones whereas the altermagnetic term induces anisotropic momentum shifts as we show below.

[54] See Supplemental Material at XXX for details about (Sec. S1) Bogoliubov Fermi Surfaces in superconducting topological altermagnets, (Sec. S2) Bogoliubov Fermi surfaces in the surface spectrum of a superconducting topological altermagnet, (Sec. S3) Topological phase transition driven by altermagnetism at the surface, and (Sec. S4) Spatial shift of Majorana zero mode in a vortex line along the x-direction, which includes Ref. [58].

[55] This 1D winding number is computed along  $k_z$ -direction for a fixed in-plane momentum  $(k_x, k_y)$ . More details can be found in the Ref. [54].

[56] C.-K. Chiu, J. C. Y. Teo, A. P. Schnyder, and S. Ryu, *Rev. Mod. Phys.* **88**, 035005 (2016).

[57] This gapless BFS demonstrates diverse topological structures, such as sphere and torus, when the chemical potential lies in the bulk bands and the condition  $t_{AM} > t_c^b = \frac{1}{2}\sqrt{\Delta^2 + (\mu - |M - t|)^2}$  is satisfied (see Ref. [54]).

[58] P. M. R. Brydon, D. F. Agterberg, H. Menke, and C. Timm, *Phys. Rev. B* **98**, 224509 (2018).

[59] C. Setty, S. Bhattacharyya, Y. Cao, A. Kreisel, and P. J. Hirschfeld, *Nat. Commun.* **11**, 523 (2020).

[60] C. Timm and A. Bhattacharya, *Phys. Rev. B* **104**, 094529 (2021).

[61] H. Oh, D. F. Agterberg, and E.-G. Moon, *Phys. Rev. Lett.* **127**, 257002 (2021).

[62] N. F. Q. Yuan and L. Fu, *Proc. Natl. Acad. Sci. U.S.A.* **119**, e2119548119 (2022).

[63] Y. Mo, X.-J. Wang, Z.-Y. Zhuang, and Z. Yan, *Phys. Rev. B* **111**, L140504 (2025).

[64] S. Smidstrup, D. Stradi, J. Wellendorff, P. A. Khomyakov, U. G. Vej-Hansen, M.-E. Lee, T. Ghosh, E. Jónsson, H. Jónsson, and K. Stokbro, *Phys. Rev. B* **96**, 195309 (2017).

[65] M. Papaj and L. Fu, *Nat. Commun.* **12**, 577 (2021).

[66] The  $\mathbb{Z}_2$  invariant can be calculated following Kitaev's formula as  $(-1)^v = \text{sgn}(\text{Pf}[iH(k_z = 0)]\text{Pf}[iH(k_z = \pi)])$  from Pfaffian of the Hamiltonian at two points.

[67] S. Qin, L. Hu, C. Le, J. Zeng, F.-c. Zhang, C. Fang, and J. Hu, *Phys. Rev. Lett.* **123**, 027003 (2019).

[68] L.-H. Hu, X. Wu, C.-X. Liu, and R.-X. Zhang, *Phys. Rev. Lett.* **129**, 277001 (2022).

[69] L.-H. Hu and R.-X. Zhang, *Nat. Commun.* **14**, 640 (2023).

[70] X.-J. Luo, X.-H. Pan, Y. Shi, and F. Wu, *Phys. Rev. B* **111**, 144501 (2025).

[71] Note that the phase region (I) also appears in superconducting vortices of doped topological insulators [72], while the phase region (IV) is unique due to the presence of altermagnetic order.

[72] P. Hosur, P. Ghaemi, R. S. K. Mong, and A. Vishwanath, *Phys. Rev. Lett.* **107**, 097001 (2011).

[73] Z. Yan, Z. Wu, and W. Huang, *Phys. Rev. Lett.* **124**, 257001 (2020).

[74] S. A. A. Ghorashi, T. L. Hughes, and E. Rossi, *Phys. Rev. Lett.* **125**, 037001 (2020).

[75] L. Fu and C. L. Kane, *Phys. Rev. Lett.* **100**, 096407 (2008).

[76] Note that the eigenstates from different  $C_{2z}$  sectors presented in Fig. 4(f) will not hybridize. Thus the MZMs are still be protected by a superconducting energy gap as large as  $\Delta$ .

[77] G. Cuono, R. M. Sattigeri, C. Autieri, and T. Dietl, *Phys. Rev. B* **108**, 075150 (2023).

[78] S. X. M. Riberolles, T. V. Trevisan, B. Kuthanazhi, T. W. Heitmann, F. Ye, D. C. Johnston, S. L. Bud'ko, D. H. Ryan, P. C. Canfield, A. Kreyssig, A. Vishwanath, R. J. McQueeney, L.-L. Wang, P. P. Orth, and B. G. Ueland, *Nat. Commun.* **12**, 999 (2021).

[79] B. Jiang, M. Hu, J. Bai, Z. Song, C. Mu, G. Qu, W. Li, W. Zhu, H. Pi, Z. Wei, Y.-J. Sun, Y. Huang, X. Zheng, Y. Peng, L. He, S. Li, J. Luo, Z. Li, G. Chen, H. Li, H. Weng, and T. Qian, *Nat. Phys.* **21**, 754 (2025).

[80] F. Zhang, X. Cheng, Z. Yin, C. Liu, L. Deng, Y. Qiao, Z. Shi, S. Zhang, J. Lin, Z. Liu, M. Ye, Y. Huang, X. Meng, C. Zhang, T. Okuda, K. Shimada, S. Cui, Y. Zhao, G.-H. Cao, S. Qiao, J. Liu, and C. Chen, *Nat. Phys.* **21**, 760 (2025).

[81] H. Reichlova, R. Lopes Seeger, R. González-Hernández, I. Kounta, R. Schlitz, D. Kriegner, P. Ritzinger, M. Lammel, M. Leiviskä, A. Birk Hellenes, K. Olejník, V. Petříček, P. Doležal, L. Horak, E. Schmoranzerova, A. Badura, S. Bertaina, A. Thomas, V. Baltz, L. Michez, J. Sinova, S. T. B. Goennenwein, T. Jungwirth, and L. Šmejkal, *Nat. Commun.* **15**, 4961 (2024).

[82] L. Han, X. Fu, R. Peng, X. Cheng, J. Dai, L. Liu, Y. Li, Y. Zhang, W. Zhu, H. Bai, Y. Zhou, S. Liang, C. Chen, Q. Wang, X. Chen, L. Yang, Y. Zhang, C. Song, J. Liu, and F. Pan, *Sci. Adv.* **10**, eadn0479 (2025).

## END MATTER

*Symmetry analysis of the AMTIs.*—The introduction of altermagnetic order fundamentally reconstructs the symmetry landscape of the system. The parent state of TIs belongs to the magnetic point group 4/mmm1', which includes all unitary crystalline symmetries of the  $D_{4h}$  point group and their products with time-reversal symmetry  $T$ .

The specific form of the altermagnetic term, which couples as a momentum-dependent Zeeman field with a  $d$ -wave symmetry, breaks time-reversal symmetry  $T$ . However, due to its compensated, non-ferromagnetic nature, it preserves a subset of symmetries that combine  $T$  with broken unitary operations. The resulting system is described by the magnetic point group 4'/m'm'm'. The fate of each symmetry operation under the introduction of altermagnetism is summarized in Table I and analyzed below.

*Topological invariants of nodal-ring semimetals and superconducting phases.*—The topological characterization of the system evolves significantly between the normal and superconducting states, and is further refined in the presence of defects such as vortices. In the normal state, the Hamiltonian of AMTIs possesses a chiral symmetry given by  $C = \rho_y$ , satisfying  $C^2 = 1$ . When the spectrum is fully gapped, the system is classified by a three-dimensional winding number:

$$w_{3D} = \int \frac{d^3\mathbf{k}}{48\pi^2} \epsilon_{abc} \text{Tr}[C\mathcal{H}^{-1}\partial_{k_a}\mathcal{H}\mathcal{H}^{-1}\partial_{k_b}\mathcal{H}\mathcal{H}^{-1}\partial_{k_c}\mathcal{H}]. \quad (4)$$

However, in the presence of gapless nodal rings, this invariant is ill-defined. The topology of the nodal structure itself is in-

$E$	$2C_{4z}$	$C_{2z}$	$2C'_2$	$2C''_2$	$\mathcal{I}$	$2S_4$	$\sigma_h$	$2\sigma_v$	$2\sigma_d$
✓	✗	✓	✗	✓	✓	✗	✓	✗	✓
$T$	$2TC_{4z}$	$TC_{2z}$	$2TC'_2$	$2TC''_2$	$\mathcal{I}T$	$2TS_4$	$T\sigma_h$	$2T\sigma_v$	$2T\sigma_d$
✗	✓	✗	✓	✗	✗	✓	✗	✓	✗

Table I. Symmetry analysis of the 4'/m'm'm' magnetic point group of the topological AMs. The table classifies all crystalline symmetries as either preserved or broken by the altermagnetic order. A checkmark (✓) indicates a symmetry that is preserved, while a cross (✗) indicates a symmetry that is broken. Symmetry operations are defined as:  $E$ , identity;  $C_{nz}$ ,  $n$ -fold rotation about  $z$ -axis;  $C'_2/C''_2$ , two-fold rotations about in-plane axes;  $\mathcal{I}$ , inversion;  $S_4$ , four-fold rotoinversion;  $\sigma_h/\sigma_v/\sigma_d$ , mirror planes;  $T$ , time-reversal. Prefixes indicate the number of symmetry-equivalent operations.

stead captured by a 1D winding number computed on a path along  $z$ -direction in momentum space. For a ring extending in the  $k_x - k_y$  plane, the invariant for a given  $(k_x, k_y)$  is

$$w_{1D}(k_x, k_y) = \int \frac{dk_z}{4\pi i} \text{Tr}[C\mathcal{H}^{-1}\partial_{k_z}\mathcal{H}]. \quad (5)$$

Introducing superconductivity and a finite chemical potential generally breaks the chiral symmetry  $C$ , precluding the use of the above invariants. A topological description can be recovered by considering a quasi-1D geometry with open boundary conditions in the  $xy$  plane and periodic boundary conditions along  $z$  direction. In this geometry, the system respects a combined anti-unitary symmetry  $\sigma_v T$ , where  $\sigma_v$  is a mirror reflection with respect to the  $xz$  or  $yz$  plane. This symmetry allows for the construction of a new chiral operator for the BdG Hamiltonian from the particle-hole symmetry  $\Xi$  and  $\sigma_v T$ , given by  $C_{1D} = \tau_z \rho_z \sigma_z$  incorporates the site mirror reflection with  $C_{1D}^2 = 1$ . The topology along the remaining periodic direction ( $k_z$ ) is then characterized by the winding number

$$w = i \int \frac{dk_z}{4\pi} \text{Tr}[C_{1D}\mathcal{H}_{\text{BdG}}^{-1}(k_z)\partial_{k_z}\mathcal{H}_{\text{BdG}}(k_z)]. \quad (6)$$

This framework can be extended to systems containing a vortex line along  $z$ . While the vortex simultaneously breaks time-reversal symmetry  $T$  and mirror symmetry  $\sigma_v$  individually, it preserves their combination  $\sigma_v T$ . Consequently, the chiral symmetry  $C_{1D}$  remains intact. The system additionally possesses a two-fold rotational symmetry  $C_{2z} = i\tau_z \sigma_z$  about the  $z$ -axis. Given that  $[C_{1D}, C_{2z}] = 0$  and  $[\Xi, C_{2z}] = 0$ , the Hamiltonian can be block-diagonalized into the two eigensectors ( $s = \pm$ ) of  $C_{2z}$ . A topological winding number can be defined within each sector using the projector  $\mathcal{P}_s = (1 + siC_{2z})/2$ :

$$w_s = i \int \frac{dk_z}{4\pi} \text{Tr}[\mathcal{P}_s C_{1D}\mathcal{H}_{\text{BdG}}^{-1}(k_z)\partial_{k_z}\mathcal{H}_{\text{BdG}}(k_z)]. \quad (7)$$

The total winding number is given by the sum over both sectors,  $w = w_+ + w_-$ . A nonzero  $w_s$  in a given sector implies the existence of topological protected vortex-bound states within that specific symmetry channel.

## SUPPLEMENTAL MATERIAL

### ABSTRACT

This Supplemental Material provides detailed analytical and numerical support for the main text, structured into four sections: In Section S1, we present a comprehensive analysis of the Fermi surface topology in an altermagnetic topological insulator and the consequent formation of symmetry-protected Bogoliubov Fermi Surfaces (BFSs) upon the introduction of  $s$ -wave superconductivity. In Section S2, we focus on the surface spectrum. Using a  $\mathbf{k} \cdot \mathbf{p}$  model and open boundary conditions, we derive the effective Hamiltonian for the topological surface states. We show that the altermagnetic term acts as a momentum shift, and determine the critical strength for the emergence of nodal surfaces in the presence of superconductivity. In Section S3, we investigate the topological phase transition in a prism nanowire geometry. We solve for the bound states and derive the exact phase boundary in the parameter space of altermagnetic strength and system size. Finally, in Section S4, we extend our analysis to vortex line along  $x$ -direction, demonstrating how the altermagnetic order induces a characteristic spatial shift of the Majorana zero mode away from the vortex core.

### S1. BOGOLIUBOV FERMI SURFACES IN BULK SPECTRUM OF A SUPERCONDUCTING TOPOLOGICAL ALTERMAGNET

In this section, we present the topological properties of Bogoliubov Fermi surfaces (BFSs) in the bulk spectrum. Let us start with the normal states phase. Figure S1(a) presents the comprehensive Fermi surface topology in altermagnetic topological insulator as a function of the mass parameter  $m$  and chemical potential  $\mu$ , for a fixed altermagnetic field strength  $t_{AM} = 0.35$ . These Fermi surfaces exhibit diverse topological configurations in momentum space, including: (i) spherical surfaces centered at high-symmetry points (HSPs), (ii) torus structures with non-trivial genus, and (iii) nested spherical shells - with the specific morphology determined by the  $(m, \mu)$  parameters.

In the presence of superconducting pairing, the altermagnetic spin splitting plays a crucial role by prohibiting the formation of conventional spin-singlet Cooper pairs between time-reversed states at momenta  $\mathbf{k}$  and  $-\mathbf{k}$ . Consequently, due to the diverse topology of the Fermi surface in a altermagnetic topological insulator, the system stabilizes various types of BFSs. As shown in Figs. S1(b) and (d), we plot the BFSs in the vicinity of HSPs for two representative cases, denoted by the purple square and hexagon in the phase diagram of Fig. S1(a). In Fig. S1(b), the normal-state Fermi surface consists of nested spheres, a result of the altermagnetic spin splitting. The superconducting pairing can only fully gap the states in the vicinity of the line defined by  $\delta k_x = \pm \delta k_y$ , where the two Fermi surfaces cross. Here,  $\delta k_i$  represents the momen-

tum deviation from the HSPs. Figure S1(c) shows a comparison of the band structure along the  $k_x$  direction: the particle (red dashed line) and hole bands (blue dashed line) in the normal state, and the Bogoliubov quasiparticle spectrum (black solid lines) in the superconducting state. This verifies that the superconducting pairing cannot open a gap where the altermagnetic spin splitting has separated the bands. In Fig. S1(d), the Fermi surface (red) exhibits a torus structure. In the presence of superconducting pairing, the resulting BFS preserves this toroidal geometry which is verified by the detailed band calculations in Fig. S1(e).

The microscopic origin of these BFSs can be understood through an effective single-band description valid near the normal-state Fermi surface. This description remains accurate under weak-coupling conditions where the pairing potential  $\Delta$  is much smaller than the direct band gap to other bands. The Bogoliubov-de Gennes (BdG) Hamiltonian in the Nambu basis is:

$$\mathcal{H}_{\text{BdG}}(\mathbf{k}) = \begin{pmatrix} \mathcal{H}_e(\mathbf{k}) & \Delta \\ \Delta & \mathcal{H}_h(\mathbf{k}) \end{pmatrix}, \quad (\text{S1.1})$$

where the hole block is related to the electron block by particle-hole symmetry:  $\mathcal{H}_h(\mathbf{k}) = -\sigma_y \mathcal{H}_e^*(-\mathbf{k}) \sigma_y$ . We use the HSP  $(0, \pi, \pi)$  from Fig. S1(d) as an example. Expanding the electron Hamiltonian  $\mathcal{H}_e(\mathbf{k})$  around this point, we obtain:

$$\mathcal{H}_e(\mathbf{k}) = (m - t) \rho_z \sigma_0 + \lambda \rho_x (k_x \sigma_x - k_y \sigma_y - k_z \sigma_z) + 2t_{AM} \rho_z \sigma_z - \mu \rho_0 \sigma_0, \quad (\text{S1.2})$$

where  $\rho_i$  and  $\sigma_i$  are Pauli matrices acting on orbital and spin space, respectively. This Hamiltonian is diagonalized as:  $\mathcal{H}_e(\mathbf{k}) \Psi_{s,\zeta}^e(\mathbf{k}) = E_{s,\zeta}^e(\mathbf{k}) \Psi_{s,\zeta}^e(\mathbf{k})$ , with the energy eigenvalues given by:

$$E_{s,\zeta}^e(\mathbf{k}) = s \sqrt{(\sqrt{(m - t)^2 + \lambda^2 k_\perp^2} + 2\zeta t_{AM})^2 + \lambda^2 k_z^2}, \quad (\text{S1.3})$$

where  $s, \zeta = \pm 1$  and  $k_\perp = \sqrt{k_x^2 + k_y^2}$ . A unitary transformation  $U = (\Psi_{++}^e, \Psi_{+-}^e, \Psi_{--}^e, \Psi_{-+}^e)$  diagonalizes the Hamiltonian:  $\mathcal{H}_e(\mathbf{k})$  is diagonalized as

$$U^\dagger \mathcal{H}_e(\mathbf{k}) U = \text{diag}(E_{++}^e(\mathbf{k}), E_{+-}^e(\mathbf{k}), E_{--}^e(\mathbf{k}), E_{-+}^e(\mathbf{k})). \quad (\text{S1.4})$$

For the hole sector, the eigenvalues and eigenvectors are related to their electronic counterparts by the particle-hole transformation:  $\mathcal{H}_h(\mathbf{k}) \Psi_{s,\zeta}^h(\mathbf{k}) = E_{s,\zeta}^h(\mathbf{k}) \Psi_{s,\zeta}^h(\mathbf{k})$  where  $E_{s,\zeta}^h(\mathbf{k}) = -E_{s,\zeta}^e(-\mathbf{k})$  and  $\Psi_{s,\zeta}^h(\mathbf{k}) = \sigma_y \Psi_{s,\zeta}^{e*}(-\mathbf{k})$  are related to the electronic states via the particle-hole transformation. Transforming into the eigenbasis of the normal state, the pairing term undergoes the same unitary transformation. A direct calculation shows that the intraband pairing matrix element vanishes:  $\langle \Psi_{s,\zeta}^e(\mathbf{k}) | \Delta | \Psi_{s,\zeta}^h(\mathbf{k}) \rangle = 0$ . This vanishing matrix element occurs because the torus-shaped Fermi surface cannot support conventional spin-singlet superconducting states with zero-momentum Cooper pairing. Consequently, the resulting

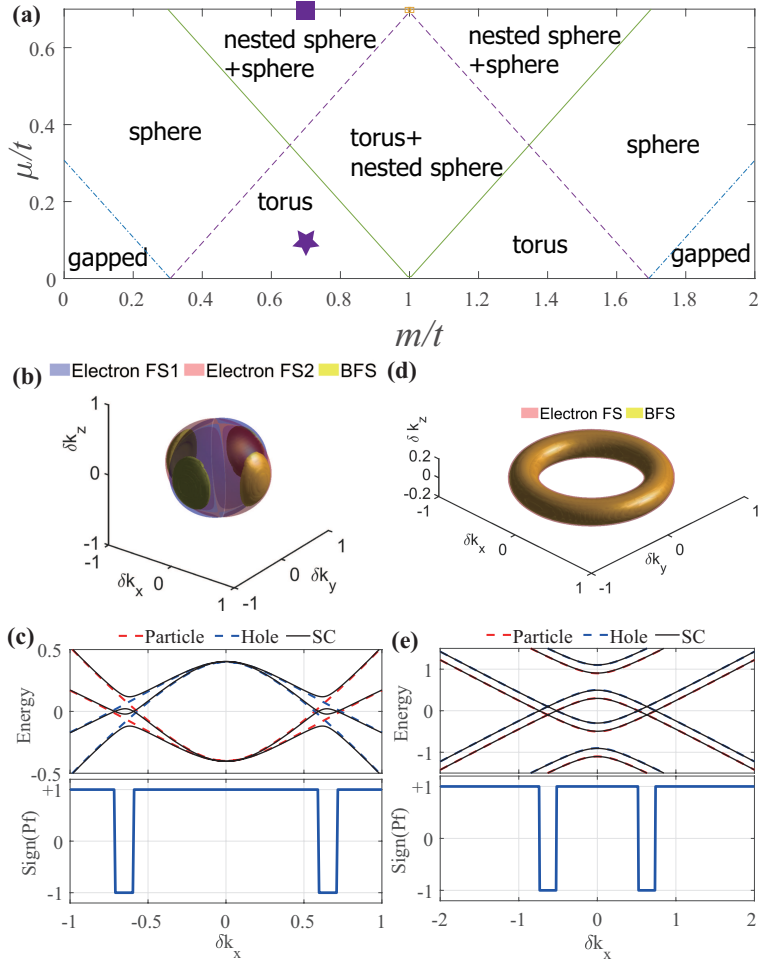


FIG. S1. (a) Fermi surface topology of the altermagnetic topological insulators as a function of the mass parameter  $m$  and chemical potential  $\mu$ . (b) Nested Fermi sphere geometry in the normal state (blue and red surfaces) and the resulting 3D BFS (yellow surfaces) centered at  $(\pi, \pi, 0)$  for  $\mu = 0.7$  [purple hexagon in (a)]. (c) Energy dispersion and Pfaffian sign along  $k_x$  in the vicinity of  $(\pi, \pi, 0)$ . Red and blue dashed curves represent the particle and hole bands in normal state, respectively. Black solid curves indicate the Bogoliubov quasiparticle spectrum. (d, e) Corresponding plots near  $(0, \pi, \pi)$  for  $\mu = 0.1$  [purple square in (a)], showing a torus Fermi surface and its associated BFS. Other parameters are  $t_{AM} = 0.35$ ,  $m = 0.7$ ,  $\Delta = 0.05$ .

BFSs precisely inherit the topology of the normal-state Fermi surface, preserving its toroidal geometry in the superconducting state. In contrast, for the nested Fermi surface case in Fig. S1(b), conventional pairing can occur in the vicinity where the Fermi surfaces intersect, allowing the superconducting gap to open in those regions.

The topological protection and classification of these BFSs are governed by two fundamental symmetries: parity ( $\mathcal{I}$ ) and particle-hole ( $\Xi$ ) symmetry. The combined  $\mathcal{I}\Xi$  symmetry enforces a  $\mathbb{Z}_2$  topological classification, where the invariant  $\nu = \text{sgn}(P(\mathbf{k}_+))\text{sgn}(P(\mathbf{k}_-))$  is computed by evaluating the relative sign of the Pfaffian at representative momenta  $\mathbf{k}_\pm$  on the two sides across the BFSs [58]. A value of  $\nu = -1$  indicates a sign change of the Pfaffian, serving as a definitive topological invariant that diagnoses the presence of a stable, symmetry-protected BFS. As shown in the bottom panels of Figs. S1(c) and (e), our calculations of the Pfaffian sign along

$k_x$  for both cases confirm that it changes sign precisely where the BFSs form.

We now derive the condition for BFS formation for arbitrary pairing strength  $\Delta$ . For  $k_z = 0$ , the Hamiltonian block-diagonalizes into sectors  $H_{+i} \oplus H_{-i}$ , corresponding to eigenvalues  $\pm i$  under the horizontal mirror operator  $\sigma_h$ . The energy spectrum for an arbitrary pairing potential  $\Delta$  is given by

$$E_\chi = 2\chi t_{AM} \pm \sqrt{\Delta^2 + (\mu \pm \sqrt{\lambda^2 k_\perp^2 + (M - t)^2})^2}, \quad (\text{S1.5})$$

where  $\chi = \pm 1$  is the sector index. Analysis of this spectrum reveals that bulk nodal crossings occur when the altermagnetic term exceeds a critical threshold,  $t_{AM} > t_{AM}^b$ , where

$$t_{AM}^b \equiv \frac{1}{2} \sqrt{\Delta^2 + (\mu - |M - t|)^2}. \quad (\text{S1.6})$$

Furthermore, crystalline symmetry guarantees that an equivalent nodal structure must appear at the  $(\pi, 0, \pi)$  point in the

Brillouin zone.

## S2. BOGOLIUBOV FERMI SURFACES IN THE SURFACE SPECTRUM OF A SUPERCONDUCTING ALTERMAGNET TOPOLOGICAL INSULATOR

In this section, we present the formation of BFSs of the surface states at physical boundaries. For concrete, we take parameters  $m = 1.5$  and  $t_{AM} < 0.25$ , for which the the system resides in a strong topological insulator phase characterized by a 3D winding number  $w_{3d} = -1$ . To obtain the edge state spectrum, we employ the  $\mathbf{k} \cdot \mathbf{p}$  model near  $(\pi, \pi, \pi)$  point. Imposing open boundary conditions along the  $y$  direction yields a Hamiltonian  $\mathcal{H} = \mathcal{H}_0(-i\partial_y) + \mathcal{H}_1$ , where

$$\mathcal{H}_0(-i\partial_y) = [(m - 3t) - \frac{t}{2}\partial_y^2]\rho_z\sigma_0 + i\lambda\partial_y\rho_x\sigma_y, \quad (\text{S2.1})$$

$$\mathcal{H}_1 = -\lambda k_x\rho_x\sigma_x - \lambda k_z\rho_x\sigma_z + \frac{1}{2}t_{AM}\partial_y^2\rho_z\sigma_z. \quad (\text{S2.2})$$

The condition  $(m - 3t)t < 0$  is necessary to guarantee the existence of edge solutions. We first seek zero-energy solutions of  $\mathcal{H}_0$  by solving  $\mathcal{H}_0\Psi = 0$ . Using the ansatz  $\Psi = \phi e^{\xi y}$ , we obtain:

$$\{[m - 3t - \frac{t}{2}\xi^2] - \lambda\xi\rho_y\sigma_y\}\phi = 0. \quad (\text{S2.3})$$

The eigenstates of  $\rho_y\sigma_y$  satisfy  $\rho_y\sigma_y\phi_\zeta = \zeta\phi_\zeta$ , which leads to the characteristic equation:

$$m - 3t - \frac{t}{2}\xi^2 - \zeta\lambda\xi = 0. \quad (\text{S2.4})$$

Solving for  $\xi$  yields:

$$\xi_{\zeta,\pm} = \frac{-\zeta\lambda \pm \sqrt{\lambda^2 + 2(m - 3t)t}}{t}. \quad (\text{S2.5})$$

Assuming  $\lambda, t > 0$ , a surface-localized solution (for  $y < 0$ ) requires  $\text{Re}(\xi_{\zeta,\pm}) > 0$ , which selects  $\zeta = -1$ . The boundary solutions are then given by:

$$\begin{aligned} |\psi_1\rangle &= \frac{1}{\sqrt{\mathcal{N}}}(e^{\xi_{-,+}y} - e^{\xi_{-,-}y})\phi_-^1, \\ |\psi_2\rangle &= \frac{1}{\sqrt{\mathcal{N}}}(e^{\xi_{-,+}y} - e^{\xi_{-,-}y})\phi_-^2, \end{aligned} \quad (\text{S2.6})$$

with the normalization factor as  $\mathcal{N} = \frac{(\xi_{-,+} - \xi_{-,-})^2}{2\xi_{-,+}\xi_{-,-}(\xi_{-,+} + \xi_{-,-})}$ . Here, the spinor components are defined as  $\phi_-^1 = |\rho_y = 1\rangle \otimes |\sigma_y = -1\rangle$  and  $\phi_-^2 = |\rho_y = -1\rangle \otimes |\sigma_y = 1\rangle$ . The matrix elements between these states are:

$$\langle\psi_2|\rho_x\sigma_x|\psi_1\rangle = 1, \langle\psi_2|\rho_x\sigma_z|\psi_1\rangle = i. \quad (\text{S2.7})$$

The altermagnetic term acts as a perturbation. Its matrix element is:

$$\langle\psi_2| - \partial_y^2\rho_z\sigma_z|\psi_1\rangle = \xi_{-,+}\xi_{-,-} = \frac{2(m - 3t)}{t}, \quad (\text{S2.8})$$

indicating that the altermagnetic term shifts the momentum of the edge states by

$$k_{AM} = -\frac{t_{AM}}{\lambda} \frac{(m - 3t)}{t}. \quad (\text{S2.9})$$

Finally, projecting the remaining terms  $\mathcal{H}_1$  onto the basis  $\{|\psi_1\rangle, |\psi_2\rangle\}$  yields the effective surface Hamiltonian:

$$\mathcal{H}_{surf} = \lambda(-k_x + k_{AM})\sigma_x - \lambda k_z\sigma_y. \quad (\text{S2.10})$$

In the presence of superconductivity, the corresponding BdG Hamiltonian is given by:

$$\mathcal{H}_{\text{BdG}} = \lambda(-k_x\tau_z + k_{AM}\tau_0)\sigma_x - \lambda k_z\tau_z\sigma_y + \Delta\tau_x, \quad (\text{S2.11})$$

where  $\tau_i$  are Pauli matrices acting in particle-hole space. For  $k_z = 0$ , the eigenenergies are

$$E_{s,\zeta} = s\lambda k_{AM} + \zeta\sqrt{\Delta^2 + (\mu - s\lambda k_x)^2} \quad (\text{S2.12})$$

with  $s, \zeta = \pm 1$ . This spectrum indicates that the surface states become nodal when the altermagnetic strength exceeds a critical value,  $t_{AM} > t_c^s$ , where

$$t_c^s \equiv \frac{\Delta}{|m - 3t|}t. \quad (\text{S2.13})$$

Figure S2 shows the band structure  $E(k_x, k_z)$  at  $k_z = \pi$  for a system with open boundaries along the  $y$ -direction. The black dashed lines represent the analytical solutions from Eq. (S2.12) (black dashed line). The numerical results show excellent agreement with the analytical model in both the subcritical  $t > t_c^s$  and supercritical  $t < t_c^s$  regimes.

## S3. TOPOLOGICAL PHASE TRANSITION DRIVEN BY ALTERMAGNETISM IN THE QUASI-1D NANOWIRE

To investigate the topological properties of the system, we analyze the quasiparticle spectrum within a triangular prism geometry, shown schematically in Fig. S3. The prism features three relevant facets: (110) and (110) and (010). The long edge of the prism is aligned parallel to the  $x$ -axis (of length  $L$ ), allowing  $k_z$  to remain a good quantum number. By conceptually cutting along the interface between the (110) and (110) surfaces and unfolding them onto a plane, we effectively map the problem to a strip geometry. This strip consists of a central region formed by the (010) surface, sandwiched between the two other surfaces. The key mechanism is the surface-projected altermagnetism: it induces a Zeeman-like splitting in the (010) surface states but vanishes on the (110) and (110) surfaces. This allows us to write an effective low-energy Hamiltonian for the strip:

$$\mathcal{H} = \mu\tau_z - i\lambda\partial_x\tau_z\sigma_x + \lambda k_z\tau_z\sigma_y + \lambda k_{AM}(x)\tau_0\sigma_x + \Delta\tau_x, \quad (\text{S3.1})$$

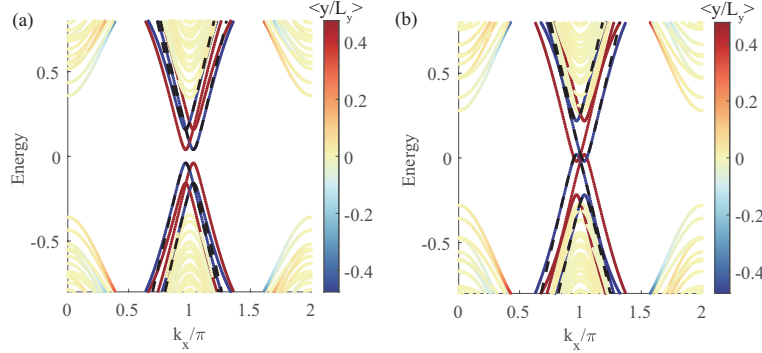


FIG. S2. Band structure  $E(k_x, k_z)$  at  $k_z = \pi$  for a system with open boundaries along the  $y$ -direction, computed for a system size  $L_y = 20$ . (a) Subcritical altermagnetic strength  $t_{AM} = 0.04$  ( $t_{AM} < t_c^s$ ). (b) Supercritical altermagnetic strength:  $t_{AM} = 0.08$  ( $t_{AM} > t_c^s$ ). The color gradient represents the spatial localization of states on the two open edges. Black dashed lines show the analytical solution from Eq. (S2.12). Parameters:  $m = 1.5$ , chemical potential  $\mu = 0.1$ , superconducting gap  $\Delta = 0.1$ .

where the altermagnetic momentum  $k_{AM}(x)$  is spatially modulated:

$$k_{AM}(x) = \begin{cases} k_{AM}, & -\frac{L}{2} < x < \frac{L}{2}; \\ 0, & \text{elsewhere.} \end{cases} \quad (\text{S3.2})$$

In this framework, we solve an eigenvalue problem to obtain the spectrum of discrete energy levels. For energies within the superconducting gap  $|\epsilon| < \Delta$ , there are no propagating states in the gapped (110) and (1̄10) regions outside the central strip. Consequently, particles incident on the interfaces at  $x = \pm L/2$  undergo only normal and Andreev reflection without transmissions. Since the bulk gap of the continuum model closes at  $k_z = 0$  as the altermagnetic strength increases, we set  $k_z = 0$  to identify the condition for gap inversion. This defines the critical boundaries between topological and trivial phases in the  $t_{AM} - L$  parameter space.

For  $k_z = 0$ , the Hamiltonian commutes with  $\sigma_x$ , allowing us to decouple the problem into two independent sectors labeled by the eigenvalue  $s = \pm 1$ .

We first find the solutions in the different regions:

(a) Central (010) surface region ( $|x| < L/2$ ,  $k_{AM} \neq 0$ ):

Within this region, for a given sector  $s$ , the Hamiltonian reduces to:

$$\mathcal{H}_s = \mu\tau_z - is\lambda\partial_x\tau_z + \lambda sk_{AM}\tau_0 + \Delta\tau_x. \quad (\text{S3.3})$$

We seek solutions of the form  $\psi = \phi e^{i\kappa x}$ , where  $\phi$  is a two-component spinor in particle-hole space. Solving the eigenvalue equation  $\mathcal{H}_s\psi_s = \epsilon\psi_s$  yields the complex wavevectors:

$$\lambda\kappa_{s,\zeta}^M = \zeta\sqrt{(\epsilon - s\lambda k_{AM})^2 - \Delta^2} - s\mu, \quad \zeta = \pm 1. \quad (\text{S3.4})$$

The corresponding eigenfunctions are:

$$|\psi_{s,\zeta}^M\rangle = \begin{pmatrix} \frac{|\epsilon - s\lambda k_{AM}| + s\zeta\sqrt{(\epsilon - s\lambda k_{AM})^2 - \Delta^2}}{\Delta} \\ 1 \end{pmatrix} e^{i\kappa_{s,\zeta}^M x}. \quad (\text{S3.5})$$

(b) Left (110) surface region ( $x < -L/2$ ,  $k_{AM} = 0$ ):

Here, the projection of altermagnetic term vanishes. We require bound state solutions that decay exponentially as  $x \rightarrow -\infty$ . The physically admissible wavevector is:

$$\lambda\kappa_s^L = -i\sqrt{\Delta^2 - \epsilon^2} - s\mu, \quad (\text{S3.6})$$

The corresponding eigenfunction is:

$$|\psi_s^L\rangle = \begin{pmatrix} \frac{-si\sqrt{\Delta^2 - \epsilon^2} + \epsilon}{\Delta} \\ 1 \end{pmatrix} e^{(\sqrt{\Delta^2 - \epsilon^2} - si\mu)x/\lambda}. \quad (\text{S3.7})$$

The imaginary part of  $\kappa_s^L$  ensures exponential decay.

(c) Right (1̄10) surface region ( $x > L/2$  and  $k_{AM} = 0$ ):

Similarly, for decay as  $x \rightarrow \infty$ , the wavevector is:

$$\lambda\kappa_s^R = i\sqrt{\Delta^2 - \epsilon^2} - s\mu. \quad (\text{S3.8})$$

The corresponding eigenfunction is:

$$|\psi_s^R\rangle = \begin{pmatrix} \frac{si\sqrt{\Delta^2 - \epsilon^2} + \epsilon}{\Delta} \\ 1 \end{pmatrix} e^{(\sqrt{\Delta^2 - \epsilon^2} - si\mu)x/\lambda}. \quad (\text{S3.9})$$

We then construct the full wavefunction and apply boundary conditions. The general wavefunction in the central region is a superposition of the left- and right-propagating (or evanescent) solutions:

$$|\Psi_s^M\rangle = \sum_{\zeta=\pm} A_{\zeta} |\psi_{s,\zeta}^M\rangle. \quad (\text{S3.10})$$

We now focus on the  $s = +1$  channel. The bound state spectrum is found by demanding that the wavefunctions are continuous at the two interfaces,  $x = \pm L/2$ . This leads to a system of equations:

$$|\Psi_s^M(-\frac{L}{2})\rangle = B|\psi_s^L(-\frac{L}{2})\rangle, \quad (\text{S3.11})$$

$$|\Psi_s^M(\frac{L}{2})\rangle = C|\psi_s^R(\frac{L}{2})\rangle.$$

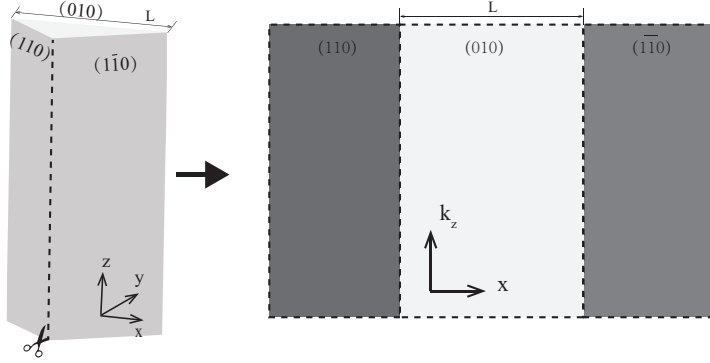


FIG. S3. Diagram illustrating the unfolding of the prism's surface.

Here,  $B$  and  $C$  are the amplitudes of the decaying waves in the left and right regions, respectively.

Next, we find the secular equation and analysis topological phase transition. This system of equations can be written in the matrix form  $\mathbf{M}\mathbf{v} = 0$  where  $\mathbf{v} = (A_+, A_-, B, C)^T$ . For a non-trivial solution to exist, the determinant of the coefficient matrix  $\mathbf{M}$  must be zero:  $\det(\mathbf{M}) = 0$ . Solving this determinant condition yields the dispersion relation for discrete energy levels:

$$\tan\left(L\sqrt{(\lambda k_{AM} - \varepsilon)^2 - \Delta^2}\right) = \frac{\sqrt{(\Delta^2 - \varepsilon^2)((\lambda k_{AM} - \varepsilon)^2 - \Delta^2)}}{\varepsilon|\lambda k_{AM} - \varepsilon| - \Delta^2} \quad (\text{S3.12})$$

The gap inversion and the emergence of topological states are signaled by the appearance of zero-energy modes ( $\varepsilon = 0$ ). Substituting  $\varepsilon = 0$  into the dispersion relation yields a simplified equation:  $\tan\left((\Delta L)\sqrt{(\frac{\lambda k_{AM}}{\Delta})^2 - 1}\right) = -\sqrt{(\frac{\lambda k_{AM}}{\Delta})^2 - 1}$  which admits solutions for the system size

$$L/\xi = \frac{n\pi - \arctan\sqrt{(k_{AM}\xi)^2 - 1}}{\sqrt{(k_{AM}\xi)^2 - 1}}, \quad (\text{S3.13})$$

where  $\xi = \lambda/\Delta$  is the superconducting coherence length and  $n = 1, 2, 3, \dots$ . This equation defines the phase boundary in the  $(t_{AM}, L)$  parameter space. Solutions to this equation exist only when  $\lambda k_{AM} > \Delta$ , confirming that the altermagnetic strength must exceed the superconducting gap to drive the system into the topological phase. The size  $L$  of the  $(010)$  facet then determines the precise quantization of the bound state energy and the number of topological modes.

#### S4. SPATIAL SHIFT OF MAJORANA ZERO MODE IN A VORTEX LINE ALONG THE X-DIRECTION

In this section, we investigate a vortex line oriented along the  $x$ -direction, where  $k_x$  remains a good quantum number. Figure S4(a) maps the minigap of this quasi-1D system in the  $(t_{AM}/\Delta, \mu/\Delta)$  parameter space. The phase diagram reveals three distinct regions: I. topological vortex line phase,

II. trivial vortex phase, and III. nodal phase. Notably, unlike the vortex along the  $z$ -direction discussed in the main text, the  $x$ -direction vortex lacks the oscillating gap regime (previously labeled IV). To understand the evolution of the topological phase, we trace a path at a fixed chemical potential of  $\mu/\Delta = 1$ , indicated by the black dashed line in S4(a). As the altermagnetic strength  $t_{AM}$  increases, the energy gap gradually closes, culminating in a nodal phase for  $t_{AM} > t_c^b$  (the white dashed line marking the phase boundary to the nodal phase (III)). Crucially, within the gapped phase, the system is characterized by a  $\mathbb{Z}_2$  topological invariant, protected by parity and particle-hole symmetry, which ensures the persistence of MZMs.

We now examine how the altermagnetic order modifies the properties of MZMs. Figures S4(b, d, f) show the energy spectra with open boundary conditions along  $x$ -direction for increasing altermagnetic strength  $t_{AM}$  ( $t_{AM}/\Delta = 0, 1, 2$ ), corresponding to the sphere, square, and hexagon markers in (a). The MZMs are highlighted by red dots. Although the bulk gap diminishes with increasing  $t_{AM}$ , the MZM remains robust at zero energy as long as the gap is finite.

The key effect of the AM field is revealed in the spatial profile of the MZM wavefunctions, shown in Figs. S4(c, e, g). At  $t_{AM} = 0$ , the MZM is tightly localized at the vortex core. As  $t_{AM}$  increases, the center of the MZM wavefunction shifts away from the core. At a sufficiently strong  $t_{AM}$ , the MZM relocates to the sample hinge. This spatial shift can be understood intuitively: The altermagnetic order acts as a momentum-dependent Zeeman field. On surfaces parallel to the  $x$ -direction, this combines with the physical magnetic field of the vortex (also along  $x$  direction). The point where the net effective field vanishes—the natural binding site for the MZM—is consequently displaced away from the geometric center. Due to the alternating sign of the altermagnetic field, adjacent side surfaces experience opposite effective Zeeman fields, resulting in opposite shifts of the MZMs on the front and back terminations.

The deviation of the MZMs from the vortex core provides a direct experimental signature for detecting AM order in superconducting topological systems. This distinct spatial shift serves as a definitive marker to distinguish altermagnetic

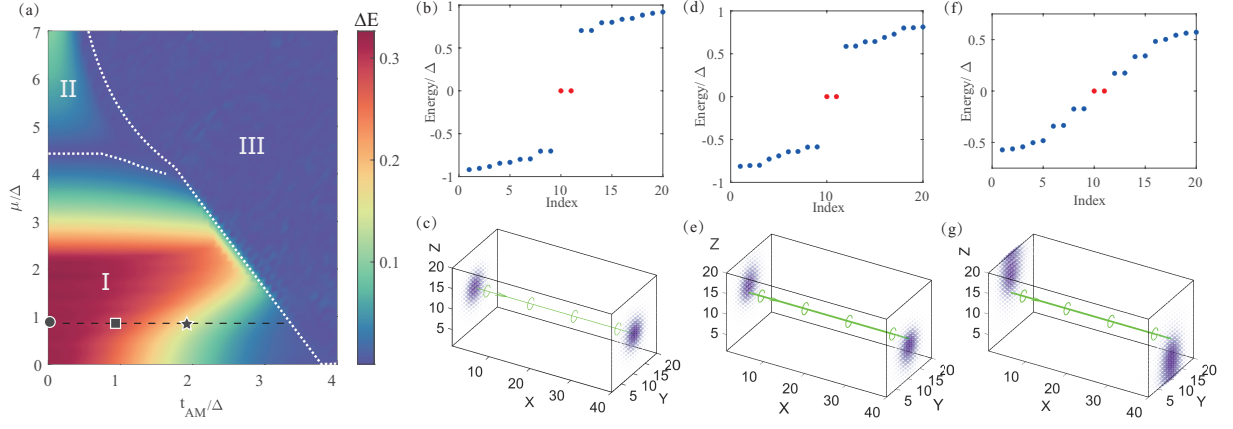


FIG. S4. (a)Topological phase diagram for a vortex line along the  $x$ -axis in the  $(t_{AM}/\Delta, \mu/\Delta)$  parameter space. The phases are labeled as follows: I. Topological vortex line phase, II. Trivial vortex phase, and III. Nodal phase. The color scale represents the minigap  $\Delta E$ . The black dashed line at  $\mu/\Delta = 1$  indicates the parameter cut for panels (b, d, f), with the sphere, square, and hexagon marking the specific values of  $t_{AM}/\Delta = 0, 1, 2$ , respectively. The white dashed line indicates the critical boundary. (b, d, f) Energy spectra under open boundary conditions in the  $x$ -direction for  $t_{AM}/\Delta = 0, 1, 2$ , respectively. Majorana zero modes are highlighted by red dots. (c, e, g) Spatial profiles of the zero-energy wavefunction magnitude for  $t_{AM}/\Delta = 0, 1, 2$ , respectively. The evolution shows the Majorana state shifting from the vortex core towards the sample hinge as the altermagnetic strength increases. Parameters:  $\Delta = 0.2$ ,  $m = 2.5$ .

vortices from conventional superconducting ones and offers

a novel mechanism for manipulating MZMs in topological quantum devices.